



The Great Dimming of Betelgeuse: A Surface Mass Ejection and Its Consequences

Andrea K. Dupree¹ , Klaus G. Strassmeier² , Thomas Calderwood³, Thomas Granzer², Michael Weber² ,
Kateryna Kravchenko⁴, Lynn D. Matthews⁵ , Miguel Montargès⁶ , James Tappin⁷, and William T. Thompson⁸

¹Center for Astrophysics | Harvard & Smithsonian, 60 Garden Street, MS-15, Cambridge, MA 02138, USA; dupree@cfa.harvard.edu

²Leibniz-Institut für Astrophysik Potsdam (AIP), An der Sternwarte 16, D-14482 Potsdam, Germany

³American Association of Variable Star Observers, 49 Bay State Road, Cambridge, MA 02138, USA

⁴Max-Planck Institut für Extraterrestrische Physik, Giessenbachstrasse 1, D-85748 Garching, Germany

⁵Massachusetts Institute of Technology, Haystack Observatory, 99 Millstone Road, Westford, MA 01886 USA

⁶LESIA, Observatoire de Paris, Université PSL, CNRS, Sorbonne Université, Université Paris Cité, 5 place Jules Janssen, F-92195 Meudon, France

⁷RAL Space, STFC Rutherford Appleton Laboratory, Harwell Campus, Didcot OX11 0QX, UK

⁸ADNET Systems Inc., NASA Goddard Spaceflight Center, Code 671, Greenbelt, MD 20771, USA

Received 2022 May 19; revised 2022 June 6; accepted 2022 June 9; published 2022 August 25

Abstract

The bright supergiant, Betelgeuse (Alpha Orionis, HD 39801), underwent a historic optical dimming during 2020 January 27–February 13. Many imaging and spectroscopic observations across the electromagnetic spectrum were obtained prior to, during, and subsequent to this dimming event. These observations of Betelgeuse reveal that a substantial surface mass ejection (SME) occurred and moved out through the extended atmosphere of the supergiant. A photospheric shock occurred in 2019 January–March, progressed through the extended atmosphere of the star during the following 11 months and led to dust production in the atmosphere. Resulting from the substantial mass outflow, the stellar photosphere was left with lower temperatures and the chromosphere with a lower density. The mass ejected could represent a significant fraction of the total annual mass-loss rate from the star suggesting that episodic mass-loss events can contribute an amount comparable to that of the stellar wind. Following the SME, Betelgeuse was left with a cooler average photosphere, an unusual short photometric oscillation, reduced velocity excursions, and the disappearance of the ~ 400 day pulsation in the optical and radial velocity for more than two years following the Great Dimming.

Unified Astronomy Thesaurus concepts: [M supergiant stars \(988\)](#); [Red supergiant stars \(1375\)](#); [Stellar mass loss \(1613\)](#); [Stellar chromospheres \(230\)](#); [Stellar atmospheres \(1584\)](#)

1. Introduction

Betelgeuse has been observed visually or photometrically for more than a century revealing its semiregular variability. This red supergiant star is nearby and large in apparent size providing a unique opportunity for an intensive and spatially resolved study of its atmosphere and surroundings—in addition to its potential as a supernova. Two principal periods of light variation occur in the star: ~ 400 days believed due to pulsation in the fundamental mode (Joyce et al. 2020) and a longer secondary period of ~ 5.6 yr (Kiss et al. 2006; Chatys et al. 2019; Stothers 2010), typical of red supergiants but currently of uncertain origin (Joyce et al. 2020). During early 2019 December, the visual magnitude of Betelgeuse became fainter than $V \sim 1$ (Guinan et al. 2019). The stellar magnitude reached a historic minimum V magnitude of ~ 1.65 between 2020 January 27 and February 13, and subsequently recovered (AAVSO 2022). The star’s appearance changed dramatically in late 2019 December and the early months of 2020, becoming substantially darker over the southern hemisphere in optical light (Montargès et al. 2021).

The following sections describe the various observations of Betelgeuse, including new temperature diagnostics and velocity measurements. We conjecture that a surface mass ejection (SME) occurred and present recently observed atmospheric consequences for the star.

2. Betelgeuse: Fundamental Parameters

Decades of observations of Betelgeuse have resulted in hundreds of measurements; a summary of recently derived fundamental parameters is given in Table 1. Current technologies, especially interferometric techniques, determine the apparent photospheric diameter as 42 mas, which is within the errors of the pioneering measurement by Michelson & Pease (1921) of 47 ± 4.7 mas. Determination of the stellar distance from parallax measures remains challenging. Because the star is large in apparent size, and the surface contains variable bright convective cells, the measurement of a parallax based on identification of the center without contemporaneous knowledge of the brightness distribution can produce discrepant results (Van Leeuwen 2007; Chiavassa et al. 2022). For the estimates following in later sections, we adopt an apparent diameter of 42 mas (Ohnaka et al. 2011), a value of 222 pc for the distance (Harper et al. 2017), and a radius of $1000 R_{\odot}$. The stellar effective temperature can be measured using a variety of diagnostics. We select a “nominal” value of 3650 ± 50 K derived through a fitting of MARCS models to spectrophotometry of the star (Levesque et al. 2005) to represent the average normal effective temperature.

Subsequent sections report many determinations of the effective temperature of Betelgeuse as the Great Dimming occurred. Analysis of the TiO molecule where signatures appear in the optical and the infrared regions has been employed in many ways to infer T_{eff} : high-resolution spectra, moderate-resolution spectra, and photometric measures. These spectra are generally modeled by assuming a grid of temperatures in the models to obtain the best agreement with observations. A detailed discussion of



Original content from this work may be used under the terms of the [Creative Commons Attribution 4.0 licence](#). Any further distribution of this work must maintain attribution to the author(s) and the title of the work, journal citation and DOI.

Table 1
Fundamental Parameters of Betelgeuse^a

Property	Value	Comment	Reference
Temperature	3650 ± 50 K	Spectrophotometry + MARCS models	1
Spectral type	M1-M2Ia-Iab	Photographic spectra	3
Radial velocity	+21.91 ± 0.51 km s ⁻¹	Integrated photospheric spectrum	2
Diameter	42.05 ± 0.05 mas	2.28–2.31 μm, uniform disk	13
Diameter	43.15 ± 0.50 mas	1.65 μm (<i>H</i> -band) limb-darkened disk	14
Diameter	125 ± 5 mas	2500 Å continuum	15
Distance	153 + 22, -17 pc	Hipparcos revised	4
Distance	168.1 + 27.5, -14.9 pc	Seismic analysis	5
Distance	222 + 48, -34 pc	Hipparcos rev. + radio positions	6
Radius	764 + 116, -62 R _⊙	Seismic analysis	5
Radius	996+215, -153R _⊙	Using Hipparcos rev. distance + radio	6
Optical variability	~0.3–1.2	Visual magnitude: 1917–2005	10
Periodicity (fundamental)	388 ± 30 days	Using visual magnitude: 1917–2005	10
Periodicity (fundamental)	420 days	Using B mag., UV cont., Mg II: 1984±1986	11
Periodicity (fundamental)	385 ± 20 days	Using radial velocity: 2008±2022	11
Secondary period	2050 ± 460 days	Using visual magnitude: 1917±2005	10
Secondary period	2229.8 ± 6 days	Using radial velocity: 2008±2022	11
Position angle north pole	48.0 ± 3.5	ALMA measurement	8
Position angle north pole	55°	Ultraviolet measurement	9

Note.

^a Extensive tables of measured parameters dating back to over a century are contained in Dolan et al. (2016).

References. (1) Levesque et al. (2005); (2) Famaey et al. (2005); (3) Keenan & McNeil (1989); (4) Van Leeuwen (2007); (5) Joyce et al. (2020); (6) Harper et al. (2017); (7) AAVSO (2022); (8) Kervella et al. (2018); (9) Uitenbroek et al. (1998); (10) Kiss et al. (2006); (11) Granzer et al. (2021); (12) Dupree et al. (1987); (13) Ohnaka et al. (2011); (14) Montargès et al. (2016); (15) Gilliland & Dupree (1996).

different procedures is given by Kravchenko et al. (2021) where these authors conclude that the bands at 6187, 7085, and 7125 Å are to be preferred because they exhibit the most sensitivity to temperature. Another technique involves the ratio of line strengths between two photospheric lines of different excitation potential, V I and Fe I. While this was calibrated for giant stars (Gray & Brown 2001), it can indicate a relative change in temperature of supergiants (Gray 2008), and is discussed in the following sections. Millimeter and centimeter observations are employed as well to determine the electron temperature in the outer atmosphere. The radio continuum in these bands results predominantly from free-free emission. Because it is thermal and optically thick, a flux measurement allows evaluation of the mean electron temperature (Reid & Menten 1997). Measures at 7 mm in 1996 suggested that the flux arises from cooler components in an inhomogeneous extended atmosphere (Lim et al. 1998), and this result is in harmony with measurements in 2019–2020.

Periodic variations in *V* magnitude and radial velocity are present. A short period of ~400 days is well documented. This period is believed to represent the fundamental pulsation mode of the supergiant (Joyce et al. 2020). The phase of the radial-velocity variation lags the phase of the *V*-magnitude variation by ~35 days (Granzer et al. 2021). The source of the much longer (~2100 days) secondary period is not established. It may represent the characteristic turnover time of giant surface convective cells (Stothers 2010).

3. Betelgeuse in 2019–2020: The Origin of the Great Dimming

3.1. The First Phase: 2019 January–November

The sequence of multifrequency observations is detailed in Table 2, including estimates of formation level of the radiation

in the atmosphere of Betelgeuse. On 2019 January 1, images of the star in the optical continuum from VLT/SPHERE revealed a roughly symmetric stellar image (Montargès et al. 2021). Tomographic study, using high-resolution HERMES optical spectra of the unresolved star (Kravchenko et al. 2021; Raskin et al. 2011) allows a probe of the dynamics of several levels in the photosphere of the supergiant. And during 2019 January, the photospheric layers exhibited the velocity signatures of a strong shock in the line of sight, and an expansion of the photospheric layers through 2019 March.

The photospheric velocity was measured continuously during this time by the automated STELLA telescopes (Granzer et al. 2021) and demonstrated that the photosphere began to expand in 2019 January and maintained a constant maximum outflowing value of -8 km s^{-1} for most of the year until 2019 mid-November, when the outward velocity began to decrease.

Optical spectra were obtained with the Tillinghast Reflector Echelle Spectrograph (TRES) mounted on the 1.5 m telescope at Fred Lawrence Whipple Observatory on Mt. Hopkins, AZ. The Ca II K-line in the lower chromosphere exhibited asymmetric emission wings signaling outflowing plasma late in 2019 January and early March (Figure 1). The extended chromosphere appeared undisturbed through early 2019, as spatially resolved UV spectra appeared similar to one other, and a “normal” (unenhanced) distribution of the chromospheric Mg II flux and ultraviolet continuum appeared across the image from 2019 January to 2019 March 5 (Dupree et al. 2020b).

From 2019 April to August, signatures of atmospheric cooling were detected. An increase in the $6 \mu\text{m}$ band is indicative of increased H₂O formation (Taniguchi et al. 2021, 2022), and both millimeter and centimeter very large array (VLA) images suggest exceptionally low temperatures, ~2400 K (Matthews & Dupree 2022).

Table 2
Spectroscopic and Imaging Observations of Betelgeuse 2019–2020

Date	Spectral Region	Formation R_{star}	Observation	Reference
2019 Jan 1	Optical image	1.0	VLT/SPHERE-ZIMPOL symmetric appearance	1
2019 Jan 1	Optical spectra	1.0	STELLA: radial-velocity outflow begins	16
2019 Jan-Apr	Optical spectra	1.0	Photospheric shock develops	2
2019 Jan 25 + Mar 5	UV spectra ^a	1.1–3	Unenhanced Mg II UV fluxes	3
2019 Jan 31 + Mar 5	Ca K spectra	~1	Outflow—low chromosphere	15
2019 Apr 1–15	6 μm Himawari	~1.1	H ₂ O increase	14
2019 Aug 2	mm—VLA image	~2.1	low T (2267 K)	4
2019 Aug 2	cm—VLA image	~2.8	low T (2583 K)	4
2019 Sep 18– Nov 28	UV spectra ^a	~1.1–3	Enhanced chromosphere (Mg II) Dense outflow/southern hemisphere	3
2019 Nov 4—Dec 8	Optical spectra	1.0	TiO temperature ~3570 K	2
2019 Dec 7	TiO, near-IR	1.0	Photometry: low T (3580 K)	11
2019 Dec 27	Optical image	1.0	VLT/SPHERE-ZIMPOL: faint southern hemisphere	1
2020 Jan 17ff	Optical spectra	1.0	V I/Fe I implies T extremely low	15
2020 Jan 2	Submm 450, 850 μm	~1	Low T (3450 K)	6
2020 Jan 28	Optical image	1.0	VLT/SPHERE-ZIMPOL: faint southern hemisphere Dust and/or cool spot	1
2020 Jan 31	Near-IR spectra	1.0	Te lower 3476 K	9
2020 Minimum	TiO: optical	1.0	Minimum value 3550 K	2
2020 Feb 3-Apr 1	UV spectrum ^a	1.1–3	Chromosphere, Mg II unenhanced	3
2020 Feb 4	10 μm Himawari	~1.2	Increased O-rich circumstellar dust	14
2020 Feb 8+19	N band/MATISSE	1.4	Localized dust and/or cool spot	12
2020 Feb 12	Optical spectra	1.0	Increased turbulence	10
2020 Feb 15	TiO; near-IR filter	1.0	$T = 3520 \pm 25$ K	5
2020 Feb 15	TiO; optical spectra	1.0	$T = 3600 \pm 25$ K	7
2020 Feb 17	X-ray	1–2	Nondetection	13
2020 Feb 23	400–740 nm	1	Aperture polarimetry; polarization from Photosphere and/or obscuration by grains	8
2020 Feb 20–Apr 2020	UV spectra ^a	1.1–3	Lower density C II chromosphere/southern hemisphere Southern hemisphere	3
2020 Mar 20	Optical image	1.0	VLT/SPHERE-ZIMPOL	8

Note.

^a Spatially resolved ultraviolet spectra (7–8 pointings across the surface).

References. (1) Montargès et al. (2021); (2) Kravchenko et al. (2021); (3) Dupree et al. (2020b); (4) Matthews & Dupree (2022); (5) Harper et al. (2020); (6) Dharmawardena et al. (2020); (7) Levesque & Massey (2020); (8) Cotton et al. (2020); (9) Alexeeva et al. (2021); (10) Zacs & Pukitis (2021); (11) Guinan et al. (2019); (12) Cannon et al. (2022); (13) Kashyap et al. (2020); (14) Taniguchi et al. (2021, 2022); (15) this paper; (16) Granzer et al. (2021).

The shock in the photosphere moved out through the extended atmosphere of the star in the months following its emergence from the surface in 2019 March–April. Here the term photosphere refers to the surface that corresponds to $1 R_{\star}$. Assuming a velocity of $5\text{--}10 \text{ km s}^{-1}$, the ejected material would reach a distance of $0.1\text{--}0.2 R_{\text{star}}$ above the photosphere in 6 months (assuming $R_{\text{star}} = 1000 R_{\text{Sun}}$; Ohnaka et al. 2011; Harper et al. 2017). This is comparable to the level where the contribution function for ultraviolet Mg II emission becomes large in semiempirical models (Lobel & Dupree 2000); moreover, Mg II continues to appear farther out in the atmosphere—up to 6 times the optical diameter (Uitenbroek et al. 1998; Dupree et al. 2020b). Assuming the shock emerged from the photosphere in 2019 March–April, a transit time of ~ 6 months is in harmony with the quiescent Mg II chromospheric emission observed in 2019 March, followed by the enhanced Mg II emission that was spatially resolved over the southern hemisphere in 2019 mid-September through 2019 November. Chromospheric emission lines of C II demonstrated the increased chromospheric density during 2019 September–November, where and when the Mg II emission was enhanced

(Dupree et al. 2020b). Such behavior signals a continuous outflow event of higher-density material.

3.2. The Historic Anomalous Phase: 2019 December–2020 March

In early 2019 December, photometry in the near-IR suggested slightly lower temperatures (~ 3580 K) were present in the photosphere than the average temperature, 3650 K (Levesque et al. 2005) or the value of ~ 3660 K found near a maximum brightness of $V \sim 0.2\text{--}0.3$ mag (Guinan et al. 2019). On 2019 December 27, imaging with SPHERE-ZIMPOL in the optical continuum near $H\alpha$ revealed a dark southern hemisphere had appeared on the star, creating a dramatic contrast with the previous image obtained on 2019 January 1 (Montargès et al. 2021).

By 2020 January 23, submillimeter spectra (Dharmawardena et al. 2020) indicated a temperature of ~ 3450 K in the photosphere, and IR spectra (Alexeeva et al. 2021) obtained 8 days later confirmed a low effective temperature of the star—this value being ~ 3476 K.

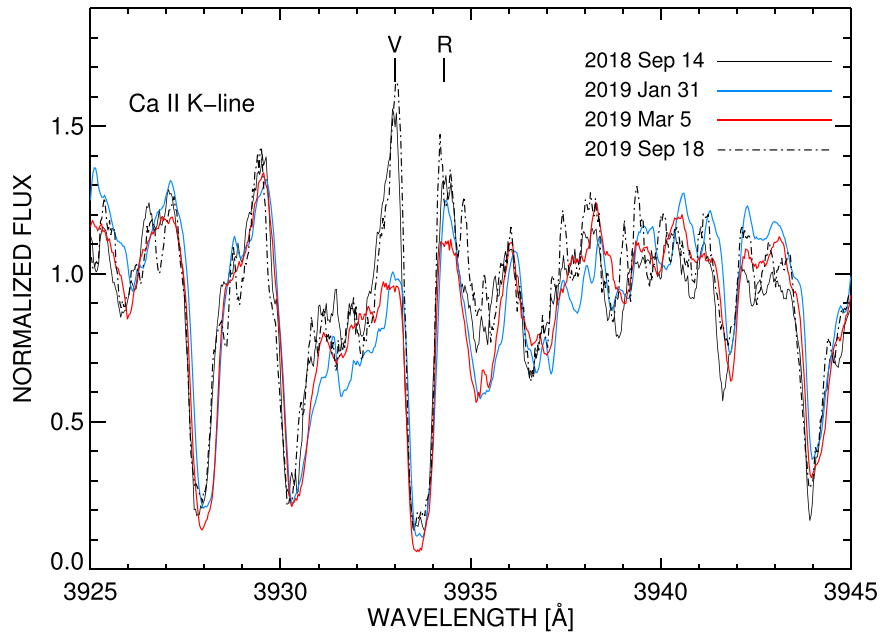


Figure 1. The chromospheric Ca II K-line, 3933 Å, from TRES echelle spectra, displays asymmetric emission wings (marked as a V (violet) and R (red) feature). The appearance of $V \leq R$ signals wind absorption from a differentially expanding atmosphere in 2019 January and March. The profile lost this asymmetry in 2019 September, mimicking the earlier profile on 2018 September 14.

Another way to determine the change in the temperature of the photosphere relies on the ratio of two atomic lines, V I ($\lambda 6251.83$) and Fe I ($\lambda 6252.5$). These features indicate the photospheric temperature in giant stars (Gray & Brown 2001), and were used to track the temperature in Betelgeuse itself (Gray 2000, 2008; Weber et al. 2009). Because the Boltzmann excitation factors differ (0.29 eV for V I and 2.40 eV for Fe I), they can serve as a temperature index. The ratio V I/Fe I becomes larger with decreasing photospheric temperature. The line-depth ratio roughly followed the V -magnitude variations of Betelgeuse for about 12 yr beginning in 1995 (Gray 2008). During that time the largest value of the ratio amounted to ~ 1.35 and corresponded to a temperature decrease of more than ~ 100 K. TRES spectra (Figure 2) obtained at the Fred Lawrence Whipple Observatory in 2019–2020 allowed measurement of this line-depth ratio, and during the Great Dimming, the variation of this ratio corresponds well with the V magnitude of the star, and it became very large (Figure 2), reaching a value of ~ 1.9 . This value suggests a larger temperature change than ~ 250 K. This value is a lower limit to T since the lines are not weak. Moreover, it appears that an adjacent line contributes to the Fe I feature at lower temperatures, suggesting that the ratio could become even larger.

The overall weakening of absorption lines from 2019 April to 2020 February 3 as shown in Figure 2, accompanied by the implied decrease in photospheric temperature is supported by spectra of other supergiant stars (Figure 3) where the T_{eff} is known (Levesque et al. 2005). For comparison, TRES echelle spectra obtained of HD 156014 ($T_{\text{eff}} = 3450$ K) and HD 175588 ($T_{\text{eff}} = 3550$ K) reveal a systematic weakening of the predominantly neutral absorption lines in this spectral region with decreasing T_{eff} .

If a large cool volume in the photosphere resulted from the SME, both the size of the cool area and the temperature differential from the rest of the atmosphere would contribute to a decrease in V magnitude. An estimate can be made of the

magnitude decrease at the maximum of the V band from a temperature of 3650 K (Levesque et al. 2005), by assuming both lowered temperatures and various surface area coverage. This shows that a 0.4 magnitude decrease occurs when 75% of the star is covered by a patch 250 K cooler than the remaining surface. A 0.5 magnitude decrease requires 90% of the star to be cooler by 250 K. Even if the cool spot temperature drops by 400 K, 60% of the star must be covered by a cool spot to achieve a 0.5 V magnitude decrease. And the photospheric temperature measures cited in Table 2 do not approach 3250 K. During the Dimming, a value of 3450 K (Alexeeva et al. 2021) is reported—a decrease of ~ 200 K. Direct imaging (Montargès et al. 2021) demonstrates that at most 50% of the star appears dimmer, perhaps only 25% as the dark area appeared in the southwest quadrant, suggesting that dust contributed to the dimming as others have suggested (Montargès et al. 2021; Cannon et al. 2022; Levesque & Massey 2020; Cotton et al. 2020; Taniguchi et al. 2022).

Now, from 2020 January 27 to February 13, the V magnitude reached a historical low level. However, on 2020 February 3 (and until 2020 April 1), the Mg II chromospheric emission and the ultraviolet continuum had returned to levels commensurate with 2019 March, which were not enhanced (Dupree et al. 2020b). Optical spectra obtained on 2020 February 12 indicated increased turbulence in the photosphere (Zacs & Pukitis 2021). On 2020 February 15, somewhat different values of T_{eff} were obtained with different diagnostics from the unresolved star. Optical TiO transitions suggested the temperature to be 3600 ± 25 K (Levesque & Massey 2020); near-IR photometry of TiO implied a slightly lower temperature of 3520 ± 25 K (Harper et al. 2020). Another analysis (Kravchenko et al. 2021) suggests that temperature diagnostics from the near-IR are to be preferred. Acceptance of that conclusion suggests that the submillimeter and near-IR measures indicate a lower temperature than usual was present in the stellar photosphere. Additionally, after passage of the dense material, the electron density in the

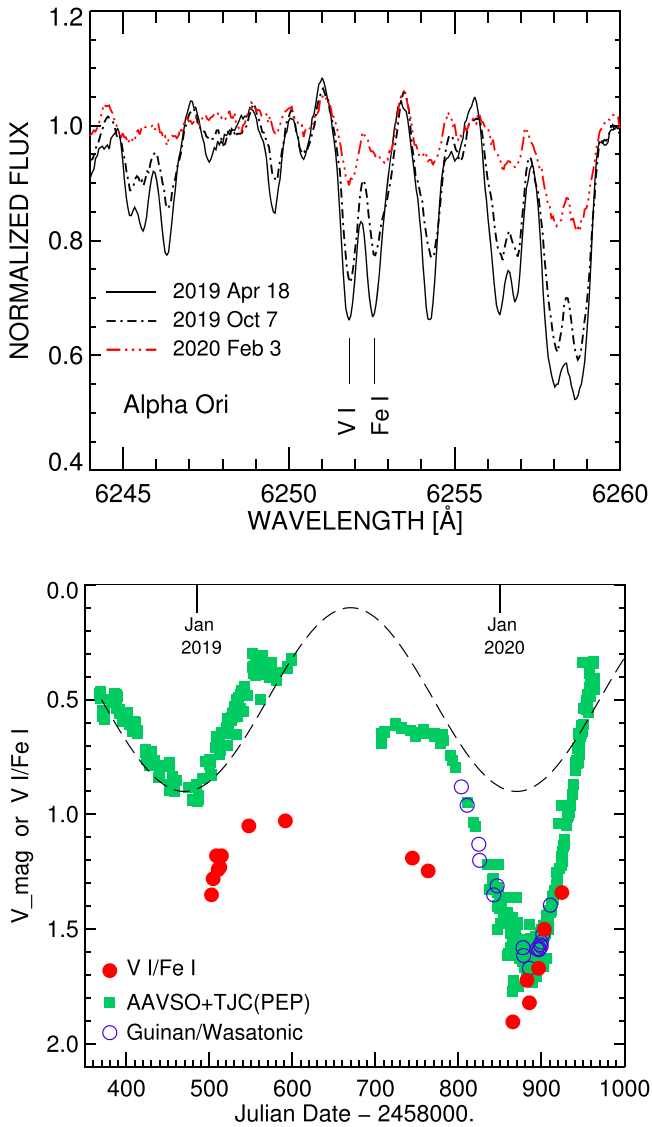


Figure 2. Top panel: three TRES echelle spectra of the temperature sensitive V I (6251.83 Å) and Fe I (6252.57 Å) absorption lines from 2019 April 18 to 2020 February 3. The Fe I line becomes weaker relative to the V I transition during this time span. Note the broadening of the Fe I line on 2020 February 3 that appears to be blended at low T (see also Figure 3). Bottom panel: the V I/Fe I depth ratios clearly follow the behavior of the V magnitude indicating a decrease of the photospheric temperature. The dashed line marks a ~ 400 day period.

southern hemisphere of the chromosphere when measured in 2020 February had returned to the lower values found in 2019 January (Dupree et al. 2020b).

Millimeter and centimeter observations with the VLA (Matthews & Dupree 2022) in 2019 August indicated substantially lower temperatures than usual: 2267 and 2583 K. It has been known for a long time that the outer atmosphere of Betelgeuse is irregular and inhomogeneous, containing both hot and cold elements. In 1996, the 7 mm radiation indicated a mean radius of 43.5 mas (Lim et al. 1998), which lies at $2 R_{\text{star}}$, clearly dispersed within warmer chromospheric plasma. Other models (Harper et al. 2001) suggest formation closer in at $1.2 R_{\text{star}}$. This region could lie near the temperature minimum above the photosphere, which semiempirical models (Lobel & Dupree 2000) suggest is located at $\sim 1.1 R_{\text{star}}$, and “below” the chromosphere. With this interpretation, the event had passed

through the submillimeter region in 2019 August leaving a cooler, less dense atmosphere. If, however, we adopt a model with columns of warm and cool material, and the warm regions are partly evacuated by the ejection event as indicated from ultraviolet observations, such an event would most likely also cause an expansion and contribute to a decrease in temperature of the remaining atmospheric material. The passage of a shock wave could lead to different effective temperatures at different atmospheric layers (Matthews & Dupree 2022).

This pattern of variation and atmospheric response suggests that an ejection event originated in the photosphere, traveled out through the extended atmosphere, eventually creating molecules and dust, as cooler regions of the extended atmosphere were reached. A disturbed local atmosphere, cooler and of lower density, remained. This would be expected when material is suddenly removed from the photosphere allowing the remaining plasma to expand and cool.

4. Solar Coronal Mass Ejections

It is helpful to review the phenomena known as coronal mass ejections (CMEs) that occur in the Sun, typically associated with solar flares. Solar CMEs result from an impulsive ejection of material, generally from the solar corona into the heliosphere (Tian et al. 2021). These plasma evacuations result in CME-induced coronal “dimming”—a weakening of coronal emission—which is attributed primarily to a decrease in the coronal density. The density decrease can last for hours following the CME (Veronig et al. 2019). Cases exist where the chromosphere is affected by a dimming as well. For instance the chromospheric He I, 10830 Å line can respond in addition to the material at coronal temperatures (Jiang et al. 2007). Study of plasma diagnostics following the event reveals additional significant effects. Construction of a differential emission measure using many ions indicates a drop in the coronal temperature of 5%–25% occurs along with the decrease in density ranging between 50% and 75% (Vanninathan et al. 2018). This solar process can inform the events observed on Betelgeuse.

5. A Surface Mass Ejection

By contrast with the Sun, Betelgeuse possesses lower gravity (by a factor of $\sim 10^4$), a substantially larger radius (by a factor of ~ 1000), and lacks the high temperatures found in the solar corona (Dupree et al. 2005; Kashyap et al. 2020). Although weak variable magnetic fields have been measured in the star (Aurière et al. 2010; Mathias et al. 2018), there is no record of flaring as found in the Sun. However, Betelgeuse is known to have a fundamental pulsation period likely driven by the κ mechanism (Joyce et al. 2020), large-scale bright variable convective cells on its surface (Haubois et al. 2009; Kervella et al. 2018; Montargès et al. 2016) that create chromospheric bright regions (Gilliland & Dupree 1996; Dupree & Stefanik 2013), and asymmetric variable large-scale chromospheric motions (Lobel & Dupree 2001). Radiative hydrodynamic simulations also suggest the presence of large vigorous convective plumes in the photosphere (Freytag et al. 2002; Chiavassa et al. 2009, 2010; Goldberg et al. 2022).

The sequence of observations discussed above suggests that Betelgeuse experienced an SME initiated by the confluence of an extended span of the outwardly moving photosphere, and the presence of shock motions likely due to a vigorous

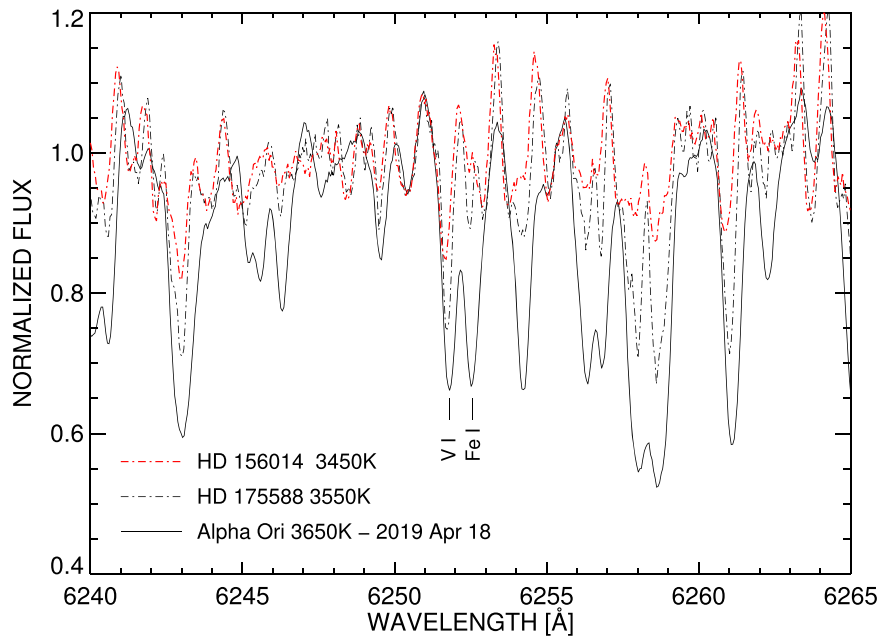


Figure 3. TRES spectra of Betelgeuse in 2019 April, a cooler supergiant (HD 156014), and a bright giant star (HD 175588). Note the systematic weakness of the absorption features as the effective temperature of the star decreases. At lower temperatures, the Fe I line at 6252.55 Å becomes blended with an unidentified absorption line. At the lowest temperature (3450 K), the unidentified line dominates the Fe I line, making the ratio measurement (V I/Fe I) in Betelgeuse a lower limit when the star is faint.

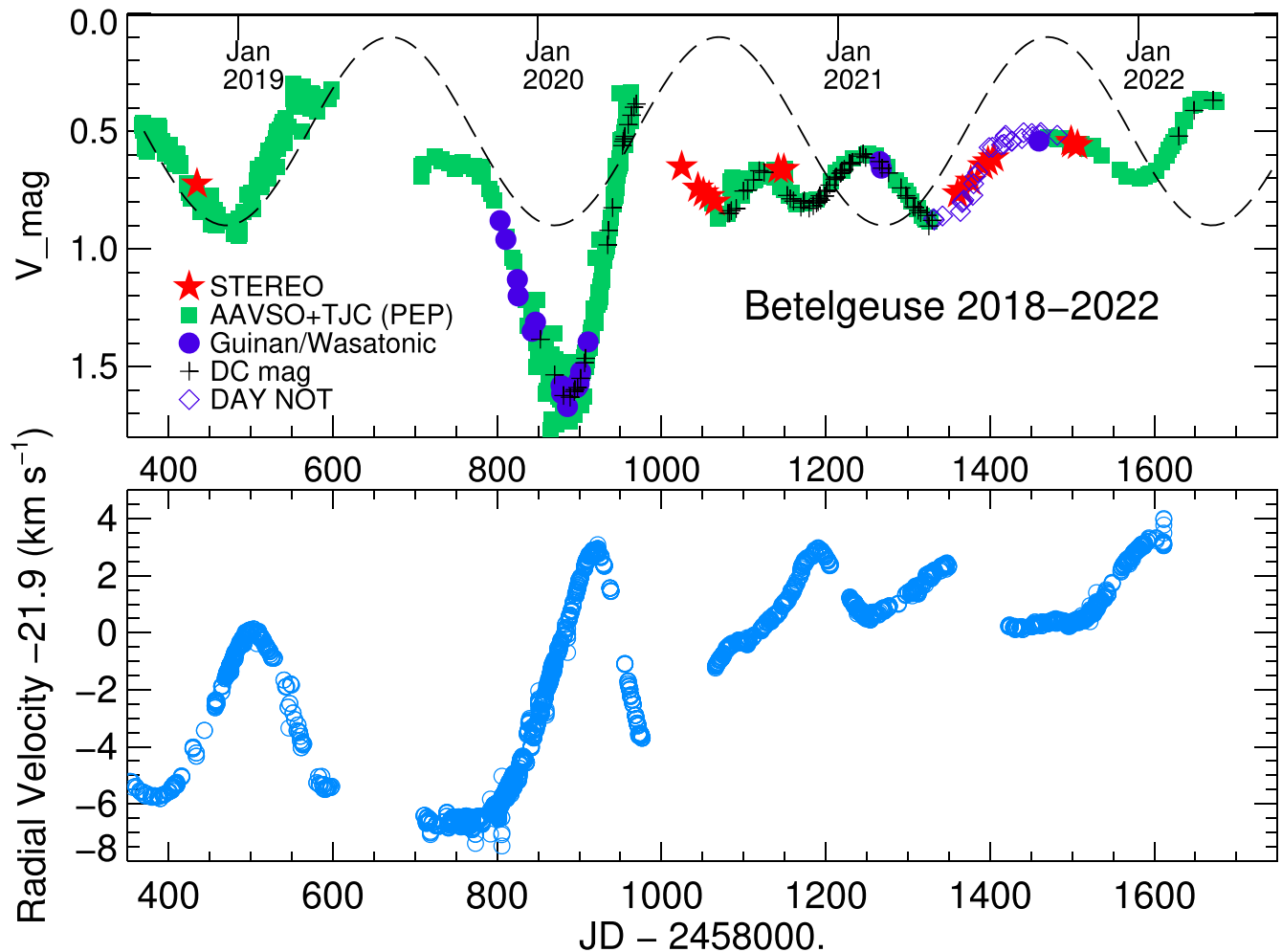


Figure 4. Top panel: V magnitude from the AAVSO (2022), STEREO, the Wasatonic Observatory, D. Corona, and daytime measures (DAY NOT). The broken line marks a ~ 400 day period. This period is no longer present after the Great Dimming. Bottom panel: radial velocity of Betelgeuse from STELLA during 2018–2022.

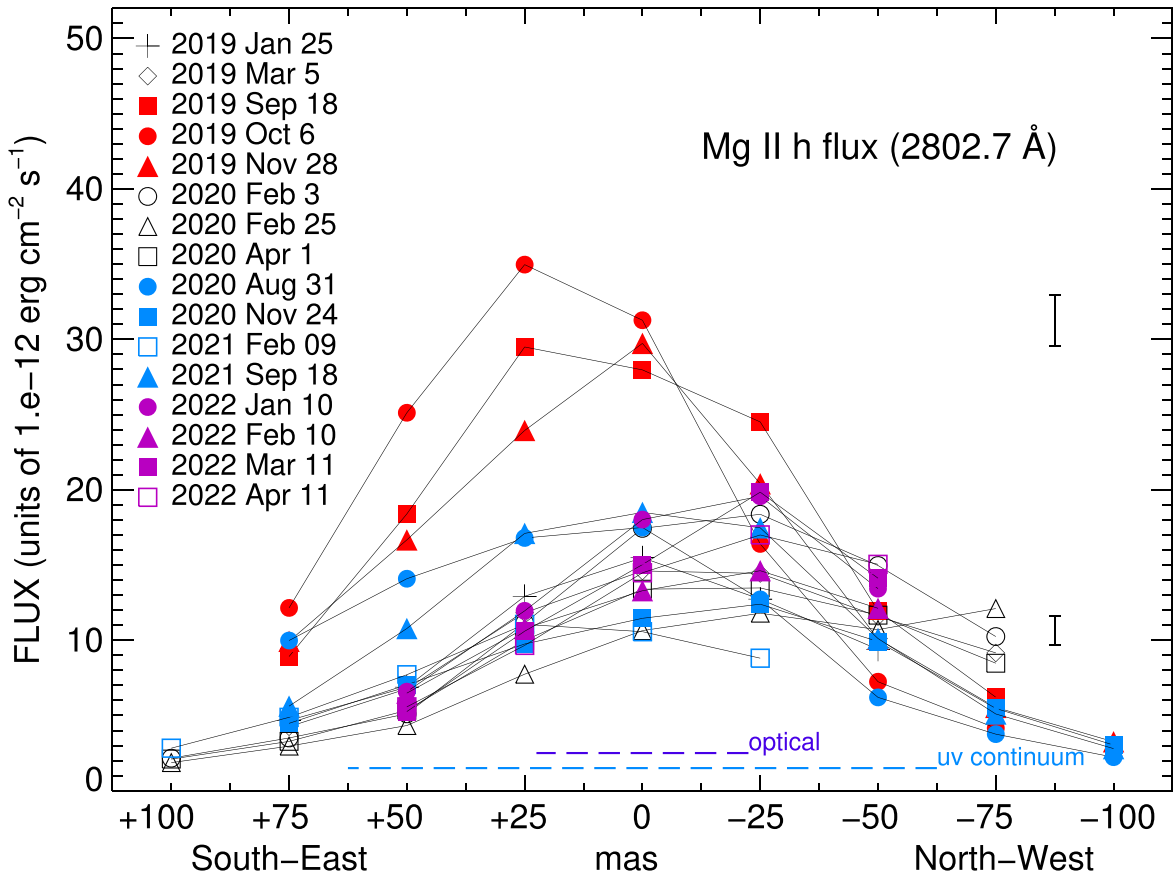


Figure 5. Mg II h flux obtained with STIS using a 25×100 mas aperture, and various offset positions. The aperture angle varies among the observations but is generally in the quadrant marked on the x -axis. The high chromospheric flux associated with the mass ejection event in 2019 September–November has not been observed subsequently. In 2022, STIS pointings were made at five positions on the disk: ± 50 mas, ± 25 mas, in the center. Optical and ultraviolet (FWHM) diameters are marked. The error bars represent the uncertainty in the STIS flux measurement.

convection cell. These combined to eject photospheric material through the chromosphere and into the extended atmosphere.

6. Betelgeuse 2021–2022: Atmospheric Response

Following the Great Dimming, Betelgeuse continued to be monitored both photometrically and spectroscopically (Figures 4 and 5). AAVSO members obtain frequent photoelectric photometer measures of the star, including some obtained during the daytime hours with multiple short exposures (Nickel & Calderwood 2021). Additionally, the Solar Terrestrial Relations Observatory spacecraft (STEREO-A) located in the Earth’s orbit but behind the Earth was rolled to repoint to Betelgeuse during the summer and fall of 2020 and 2021. The procedure is described elsewhere (Dupree et al. 2020a). An updated change in the sensitivity of the outer Heliospheric Imager HI-2, was used to extract the V magnitude in 2021 relative to the measures in 2020 (Tappin et al. 2022). These values agree well with the daylight measurements reported by the AAVSO.

Inspection of the V -magnitude variation subsequent to the Great Dimming (Figure 4) reveals dramatic changes from the well-documented ~ 400 day pulsation (Kiss et al. 2006). The periodicity has shortened substantially. After the Great Dimming, the next minimum followed in ~ 189 days, but minima in the following two years are separated by about 97, 166, and 233 days—all values clearly less than the dominant ~ 400 day pulsation period. Detailed study of periodicities in

the V magnitude spanning 88 yr (Kiss et al. 2006) identified two dominant periods: 388 ± 30 days and 2050 ± 460 days. Photometric observations over 15 yr indicated a fundamental period of 416 ± 24 days (Joyce et al. 2020). A short period of ~ 200 days resulted from analysis of a 9.8 yr study of magnitude variations (Percy et al. 1996). The surprising variable periodicity observed subsequent to the Great Dimming appears to have resulted from the rearrangement of the photosphere that followed the mass ejection and that was subjected to the presence of the underlying fundamental 400 day pulsation.

Optical spectra continued to be acquired with the STELLA echelle spectrograph (SES) on the robotic 1.2 m STELLA-II telescope located at the Izaña Observatory on Tenerife in the Canary Islands (Strassmeier et al. 2010). These spectra span 390 nm to 870 nm with a spectral resolution of 55,000 (3 pixel sampling). Standard reduction procedures were carried out with an IRAF-based pipeline (Weber et al. 2008, 2012). Wavelength calibration was made using Th-Ar lamp spectra that are obtained consecutively. After correction for the echelle blaze, radial velocities were derived using 62 of the 82 echelle orders. The very short wavelength regions with weak signals were excluded along with orders containing very strong lines (e.g., Balmer series) and orders with heavy telluric contamination. Cross correlations were made with a spectral template corresponding to 3500 K, $\log g = 0$, and standard metallicity. An order by order (for 62 orders) cross correlation utilized the template spectrum calculated with the Turbospectrum synthesis

code (Alvarez & Plez 1998) with MARCS models (Gustafsson et al. 2008) and VALD3 line lists (Ryabchikova et al. 2015). The cross-correlation functions are combined, and the final velocity is derived by fitting a Gaussian curve to the peak. The internal radial velocity error is estimated with a Monte Carlo-like approach, using 1000 different subsets of the 62 orders and generally average to 10 m s^{-1} (Granzer et al. 2021).

The photospheric radial velocity measured by STELLA (Granzer et al. 2021) also changed dramatically following the Great Dimming (Figure 4). The amplitude is much smaller ($\sim 5 \text{ km s}^{-1}$) starting in 2020 September, as contrasted with $\sim 10 \text{ km s}^{-1}$ measured previously, and the outflow is minimal or absent. The long-standing pattern of maximum radial-velocity inflow that follows the optical minimum by ~ 35 days for the past decade (Granzer et al. 2021) is not present during 2020 August, but may have returned by 2020 December. Spatially resolved ultraviolet observations with the Hubble Space Telescope continue through 2020–2022 (Figure 5), and the Mg II flux in 2022 is considerably lower than 2019 September–November and appears unenhanced.

7. Discussion

The sequence of events described earlier suggests that Betelgeuse experienced an SME. Consequences of the dimming event clearly affected the atmosphere of the star. The optical variation following the dimming is dissimilar from period changes found in giant stars such as Mira variables where period jitter of a few percent is common (Lombard & Koen 1993), or the period may decrease systematically (Zijlstra et al. 2002), or mode switching may occur (Bedding et al. 1998).

Betelgeuse undergoes substantial mass loss in a wind, and clumps of dust in its environment suggest that material has been ejected in past events (Kervella et al. 2011; Humphreys & Jones 2022). Depending on assumptions, mass-loss estimates causing the Great Dimming range from 3% to 128% of the stellar wind mass-loss rate (Montargès et al. 2021). These phenomena offer opportunities for mass loss in both continuous and eruptive fashion. It will be of interest to search the circumstellar region to the south of the star to detect evidence of this mass-loss event. At a nominal speed of 10 km s^{-1} , in 4 yr from the photospheric ejection in 2019 the material should be 38 to 48 mas distant from the stellar surface assuming pure radial motion on the sky and depending on the distance of Betelgeuse (Joyce et al. 2020; Harper et al. 2017). The apparent separation of the ejecta would be larger than the ALMA beam size at 18 mas at 0.88 mm (Kervella et al. 2018).

An analysis (Goldberg 1984) of measurements of magnitude and radial velocity led to the speculation that major disturbances in the atmosphere of Betelgeuse were likely to follow the minimum (maximum outflow) in the 6 yr radial-velocity variation. This prediction of a disturbance in 1984 did not take place, and the span of optical variability was only 0.6 mag during that time (Percy et al. 1996). The historic optical minimum in 2020 did follow the minimum in the long-term radial-velocity variation (2229.8 ± 6 days) by approximately 300 days (Granzer et al. 2021). This long period is expected to reach a minimum again in 2025 May, and perhaps in early 2026, another event may occur.






This research is supported in part by HST/STScI grant HST-GO-15641 and grant HST-GO-16655 to the Smithsonian

Astrophysical Observatory. We would like to thank the STEREO/SECCHI science team at the Naval Research Laboratory and other locations, particularly Lynn Hutting, for setting up the special observing sequences, and the STEREO Mission Operations team at the Johns Hopkins University Applied Physics Laboratory for the special roll maneuvers needed to observe Betelgeuse while the star was unobservable from Earth due to solar interference.

All of the HST data presented in this paper were obtained from the Mikulski Archive for Space Telescopes (MAST) at the Space Telescope Science Institute. The specific observations analyzed can be accessed via <https://doi.org/10.17909/92a9-9662>.

Facilities: AAVSO, FLWO(TRES), HST(STIS), STELLA (SES), STEREO(HI).

ORCID iDs

Andrea K. Dupree  <https://orcid.org/0000-0002-8985-8489>
 Klaus G. Strassmeier  <https://orcid.org/0000-0002-6192-6494>
 Michael Weber  <https://orcid.org/0000-0002-7032-2967>
 Lynn D. Matthews  <https://orcid.org/0000-0002-3728-8082>
 Miguel Montargès  <https://orcid.org/0000-0002-7540-999X>

References

- AAVSO 2022, Photometric data, www.aavso.org
 Alexeeva, S., Zhao, G., Gao, D.-Y., et al. 2021, *NatCo*, **12**, 4719A
 Alvarez, R., & Plez, B. 1998, *A&A*, **330**, 1109
 Aurière, M., Donati, J. F., Konstantinova-Antova, R., et al. 2010, *A&A*, **516**, L2
 Bedding, T. R., Zijlstra, A. A., Jones, A., & Foster, G. 1998, *MNRAS*, **301**, 1073
 Cannon, E., Montargès, M., de Koter, A., et al. 2022, *A&A*, submitted
 Chatys, F. W., Bedding, T. R., Murphy, S. J., et al. 2019, *MNRAS*, **487**, 4832
 Chiavassa, A., Haubois, X., Young, J. S., et al. 2010, *A&A*, **515**, A12
 Chiavassa, A., Kudritski, R., Davies, B., Freytag, B., & deMink, S. E. 2022, *A&A*, **661**, L1
 Chiavassa, A., Plez, B., Josselin, E., & Freytag, B. 2009, *A&A*, **506**, 1351
 Cotton, D. V., Bailey, J., DeHorta, A. Y., et al. 2020, *RNAAS*, **4**, 39
 Dharmawardena, T. E., Mairs, S., Scicuna, P., et al. 2020, *ApJ*, **897**, L9
 Dolan, M. M., Mathew, G. J., Lam, D. D., et al. 2016, *ApJ*, **819**, 7
 Dupree, A. K., Baliunas, S. L., Guinan, E. F., et al. 1987, *ApJ*, **317**, L85
 Dupree, A. K., Guinan, E., Thompson, W. T. & STEREO/SECCHI/HI consortium 2020a, *ATel*, **13901**
 Dupree, A. K., Strassmeier, K. G., Matthews, L. D., et al. 2020b, *ApJ*, **899**, 68
 Dupree, A. K., Lobel, A., Young, P. R., et al. 2005, *ApJ*, **622**, 629
 Dupree, A. K., & Stefanik, R. 2013, in *Betelgeuse Workshop 2012*, European Astronomical Society Publication Ser., 60, ed. P. Kervella et al. (Les Ulis: EDP Sciences), 77
 Famaey, B., Jorissen, A., Luri, X., et al. 2005, *A&A*, **430**, 165
 Freytag, B., Steffen, M., & Dorch, B. 2002, *AN*, **323**, 213
 Gilliland, R. L., & Dupree, A. K. 1996, *ApJ*, **463**, L29
 Goldberg, J. A., Jiang, Y.-F., & Bildsten, L. 2022, *ApJ*, **929**, 156
 Goldberg, L. 1984, *PASP*, **96**, 366
 Granzer, T., Weber, M., Strassmeier, K. G., & Dupree, A. K. 2021, in *The Cambridge Workshop on Cool Stars, Stellar Systems, and the Sun*, **20.5**, 41
 Gray, D. F. 2000, *ApJ*, **532**, 487
 Gray, D. F. 2008, *ApJ*, **135**, 1450
 Gray, D. F., & Brown, K. 2001, *PASP*, **113**, 399
 Guinan, E. F., Wasatonic, R. J., & Calderwood, T. J. 2019, *ATel*, **13341**
 Gustafsson, B., Edvardsson, B., Eriksson, L., et al. 2008, *A&A*, **486**, 951
 Harper, G. B., Brown, A., & Li, J. 2001, *ApJ*, **251**, 1073
 Harper, G. M., Brown, A., Guinan, E. F., et al. 2017, *AJ*, **154**, 11
 Harper, G. M., Guinan, E. F., Wasatonic, R., & Ryde, N. 2020, *ApJ*, **905**, 34
 Haubois, X., Perrin, G., Lacour, S., et al. 2009, *A&A*, **508**, 923
 Humphreys, R. M., & Jones, T. J. 2022, *AJ*, **163**, 103
 Jiang, Y., Yang, L., Li, K., & Ren, D. 2007, *ApJ*, **662**, L131
 Joyce, M., Leung, S.-C., Molnár, L., et al. 2020, *ApJ*, **902**, 63
 Kashyap, V. L., Drake, J. J., & Patnaude, D. 2020, *ATel*, **13501**
 Keenan, P. C., & McNeil, R. C. 1989, *ApJS*, **71**, 245

- Kervella, P., Decin, L., Richards, A. M. S., et al. 2018, *A&A*, **609**, A67
- Kervella, P., Perrin, G., Chiavassa, A., et al. 2011, *A&A*, **531**, A117
- Kiss, L. L., Szabo, Gy. M., & Bedding, T. R. 2006, *MNRAS*, **372**, 1721
- Kravchenko, L., Jorissen, A., VanEck, S., et al. 2021, *A&A*, **650**, L17
- Levesque, E. M., & Massey, P. 2020, *ApJ*, **891**, L37
- Levesque, E. M., Massey, P., Olsen, K. A. G., et al. 2005, *ApJ*, **628**, 973
- Lim, J., Carilli, C. L., White, S. M., Beasley, A. J., & Marson, R. G. 1998, *Natur*, **392**, 575
- Lobel, A., & Dupree, A. K. 2000, *ApJ*, **545**, 454
- Lobel, A., & Dupree, A. K. 2001, *ApJ*, **558**, 815
- Lombard, F., & Koen, C. 1993, *MNRAS*, **263**, 309
- Mathias, P., Aurière, M., López Ariste, A., et al. 2018, *A&A*, **615**, A116
- Matthews, L. D., & Dupree, A. K. 2022, *AJ*, in press
- Michelson, A. A., & Pease, F. G. 1921, *ApJ*, **53**, 249
- Montargès, M., Cannon, E., Lagadec, E., et al. 2021, *Natur*, **594**, 365
- Montargès, M., Kervella, P., Perrin, G., et al. 2016, *A&A*, **588**, 130
- Nickel, O., & Calderwood, T. 2021, *JAAVSO*, **49**, 269
- Ohnaka, L., Weigelt, G., Millour, F., et al. 2011, *A&A*, **529**, A163
- Percy, J. R., Desjardins, A., Yu, L., & Landis, H. J. 1996, *PASP*, **108**, 139
- Raskin, G., van Winkel, H., Hensberge, H., et al. 2011, *A&A*, **526**, A69
- Reid, M. J., & Menten, K. M. 1997, *ApJ*, **476**, 327
- Ryabchikova, T., Piskunov, N., Kurucz, R. L., et al. 2015, *PhyS*, **90**, 054005
- Stothers, R. B. 2010, *ApJ*, **725**, 1170
- Strassmeier, K. G., Granzer, T., & Weber, M. 2010, *AdAst*, **2010**, 970306
- Taniguchi, D., Yamazaki, K., & Uno, S. 2021, in European Astronomical Society Annual Meeting, SS22b, 1708, <https://eas.kuoni-congress.info/2021/programme/pdf/paperToPdf.php?id=1708>
- Taniguchi, D., Yamazaki, K., & Uno, S. 2022, *NatAs*
- Tappin, S. J., Eyles, C. J., & Davies, J. A. 2022, *SoPh*, **297**, 37
- Tian, H., Harra, L., Baker, D., Brooks, D. H., & Xia, L. 2021, *SoPh*, **296**, 47
- Uitenbroek, H., Dupree, A. K., & Gilliland, R. L. 1998, *AJ*, **116**, 2501
- Van Leeuwen, F. 2007, *A&A*, **474**, 653
- Vanninathan, K., Veronig, A. M., Dissauer, K., & Temmer, M. 2018, *ApJ*, **857**, 62
- Veronig, A. M., Gömöty, P., Dissauer, K., Temmer, M., & Vanninathan, K. 2019, *ApJ*, **879**, 85
- Weber, M., Carroll, T., Granzer, T., Steffen, M., & Strassmeier, K. G. 2009, *MmSAI*, **80**, 743W
- Weber, M., Granzer, T., & Strassmeier, K. G. 2012, *Proc. SPIE*, **8451**, 84510K
- Weber, M., Granzer, T., Strassmeier, K. G., & Woche, M. 2008, *Proc. SPIE*, **7019**, 70190L
- Zacs, L., & Pukitis, K. 2021, *RNAAS*, **5**, 8
- Zijlstra, A. A., Bedding, T. R., & Mattei, J. A. 2002, *MNRAS*, **334**, 498